Draft version October 18, 2022
Typeset using LaTeX **twocolumn** style in AASTeX631

Characterization of Population III Stars with Stellar Atmosphere and Evolutionary Modeling and Predictions of their Observability with the James Webb Space Telescope

Mikaela M. Larkin,[1] Roman Gerasimov,[1] and Adam J. Burgasser[1]

[1] *Center for Astrophysics and Space Sciences, University of California San Diego, La Jolla, CA 92093, USA*

(Received TBD; Revised October 18, 2022; Accepted TBD)

Submitted to ApJ

ABSTRACT

Population III stars were the first stars to form after the Big Bang, and are believed to have made the earliest contribution to the metal content of the universe beyond the products of the Big Bang Nucleosynthesis. These stars are theorized to have had extremely short lifespans, and therefore would only be observable at high redshifts ($z \geq 3-17$) and faint apparent magnitudes ($m_{AB} \gtrsim 40$). The direct detection of Population III stars therefore remains elusive. However, the recently launched James Webb Space Telescope (JWST) may be capable of detecting stars in the relevant magnitude range in the event of favorable gravitational lensing. Theoretical models are required to interpret these future observations. In this study, new evolutionary models and non-equilibrium model atmospheres were used to characterize the observable properties of zero-age main sequence Population III stars. The calculated models cover a wide range of possible Population III stellar masses, from the minimum mass predicted by star formation studies to the maximum mass capable of maintaining hydrostatic equilibrium. Synthetic photometry and theoretical color-magnitude diagrams were calculated for the bands of the Near-Infrared Camera (NIRCam) on JWST. The final results are compared to the scales of known lensing events and JWST magnitude limits. The purpose of this study is to calculate the observable parameters of Population III stars in the most optimal JWST bands in order to provide a theoretical foundation for anticipated future observations of this stellar population.

Keywords: Population III stars (1285) — Gravitational lensing (670) — Theoretical models (2107) — Limiting magnitude (923) — Proton-proton cycle (1299) — CNO cycle (194)

1. INTRODUCTION

Population III stars are an elusive addition to the two traditional stellar populations identified in Baade (1944). This yet unobserved population accommodates the earliest and nearly metal-free stars that formed shortly after the Big Bang. Nearly seven decades ago, Schwarzschild & Spitzer (1953) recognized that early stars were likely more massive, luminous and short-lived compared to their present-day Population I and II counterparts. The need for a non-standard formation mechanism to produce such stars and the relatively high metallicity measured in the most metal-poor Population II stars known at the time ([Fe/H] ≈ -3, Bond 1980) led Antonov & Chernin (1977)[1] and Wagner (1978) to independently identify the earliest stars as a distinct stellar population. In addition to the earliest chemical enrichment of the primordial gas, Population III stars may have contributed to the cosmic microwave background (Rowan-Robinson 1983), the cosmic infrared background (Santos et al. 2002; Kashlinsky et al. 2005; Madau & Silk 2005; Kashlinsky 2005), the gravitational wave background (Suwa et al. 2007; Kowalska et al. 2012; Kinugawa et al. 2014), reionization and

Corresponding author: Mikaela M. Larkin
mmlarkin16@gmail.com

---

[1] Note that the argument in Antonov & Chernin (1977) is based on the assumption that dark matter is composed of low-mass stars and brown dwarfs which has been largely ruled out (Bahcall et al. 1994; Graff & Freese 1996; Freese 2017).

reheating of the universe (Haiman & Loeb 1997; Cojazzi et al. 2000; Cen 2003a; Wyithe & Loeb 2003; Sokasian et al. 2004; Maio et al. 2016) and likely had a noticeable feedback effect on the formation of the first galaxies (Greif et al. 2010; Abe et al. 2021).

Recent searches for extremely metal-poor stars have revealed a sharp cut-off in the metallicity distribution around $[\mathrm{Fe/H}] \approx -4$, with fewer than 50 known objects below this cut-off (Abohalima & Frebel 2018). These include the most metal-poor star known ($[\mathrm{Fe/H}] = -6.2$, Nordlander et al. 2019) as well as at least one object with an unmeasured iron abundance and the estimated upper limit $[\mathrm{Fe/H}] \lesssim -7$ (Keller et al. 2014). However, the comparatively high abundances of other chemical elements (e.g. $[\mathrm{C/H}] \gg -3$ for both stars) challenge the status of these sources as true Population III representatives, unless the observed abundances are acquired from the interstellar medium through selective accretion, as proposed by Johnson (2015).

The lack of identifiable metal-free stars in surveys is consistent with the long-standing theoretical expectation of a top-heavy initial mass function (IMF) that precludes primordial stars from having sufficiently long lifespans to survive until the present day. This expectation is motivated by the lack of metals in the early universe, which leaves H_2 and HD as the only available cooling agents in molecular clouds, thereby suppressing fragmentation and producing unusually heavy stars (Larson 1998; Maio et al. 2010). Early numerical simulations (e.g. Abel et al. 2000; Bromm et al. 2002; Yoshida et al. 2006) suggested that Population III stars predominantly formed with masses in excess of 100 $M_\odot$ and collapsed into black holes, with the exception of a subset of stars with masses between 140 $M_\odot$ and 260 $M_\odot$ that produced pair-instability supernovae (Schneider et al. 2002; Heger & Woosley 2002). Later studies with a more detailed treatment of radiative feedback, interactions between stars, turbulence, etc., have challenged this picture by allowing formation of $\gtrsim 10$ $M_\odot$ Population III stars (e.g. Hosokawa et al. 2011; Stacy et al. 2012; Hirano et al. 2015, 2014) or even < 1 $M_\odot$ stars (e.g. Stacy et al. 2016; Susa et al. 2014; Greif et al. 2011; Clark et al. 2011) that may exist in the present-day Milky Way, likely disguised by metal-enriched mass transfer from heavier stars (Stacy & Bromm 2014). The existence of lower-mass primordial stars enables additional mechanisms of chemical enrichment, potentially explaining the observed inconsistency of the abundance patterns in metal-poor stars with predictions of pair-instability supernova yields (Umeda & Nomoto 2002). A distinct hypothetical population of supermassive primordial stars with masses in excess of $10^3 - 10^6$ $M_\odot$ has also been proposed as seeds for the supermassive black holes in high-redshift quasars (Fuller et al. 1986; Muñoz et al. 2021; Woods et al. 2021; Herrington et al. 2022).

Since the majority of Population III stars are expected to have masses between a few tens and a few hundred solar masses, the correspondingly short lifespans ($\lesssim 20$ Myr, Windhorst et al. 2018) necessitate direct observation of such objects at high redshifts. The first stars begin to form once the primordial molecular clouds, concentrated around growing dark matter over-densities, cool down sufficiently to become unstable against gravitational collapse. The star formation rate as a function of redshift can be traced in simulations of cosmological hydrodynamics (Xu et al. 2013; Wise et al. 2012b,a; Jaacks et al. 2019). The first Population III stars are expected to form around $z \approx 30$ (~ 0.1 Gyr after the Big Bang) and the maximum formation rate density ($\sim 10^{-4} - 10^{-3}$ $M_\odot$ yr^{-1} Mpc^{-3}) is attained around $17 \lesssim z \lesssim 10$ ($\sim 0.2 - 0.5$ Gyr after the Big Bang). This result is generally consistent with early reionization optical depth measurements from the Wilkinson Microwave Anisotropy Probe (WMAP) (Spergel et al. 2003; Kogut 2003; Cen 2003b), although later WMAP (Bennett et al. 2013) and Planck (Planck Collaboration et al. 2016) measurements have cast doubt on the usability of this parameter as a probe of primordial star formation (Yung et al. 2020). Population III stars give way to Population II stars once the metal mass fraction (Z) of the interstellar medium reaches a critical value, $Z_{\mathrm{cr}} \gtrsim 10^{-8} - 10^{-6}$ ($Z_{\mathrm{cr}} \gtrsim 10^{-6} Z_\odot - 10^{-4} Z_\odot$[2]; Bromm et al. 2001a; Omukai et al. 2005; Schneider et al. 2006; Clark et al. 2008; Sharda & Krumholz 2022) that allows for efficient cooling and fragmentation of collapsing molecular clouds. The lowest redshift at which Population III stars may be observed remains uncertain as isolated metal-free pockets may last for extended periods of time, producing new Population III stars at later epochs. Population III star formation is expected to continue until at least $z = 6$ (~ 1 Gyr after the Big Bang, Trenti et al. 2009; Muratov et al. 2013) and possibly much later under special circumstances (Liu & Bromm 2020). Searching for metal-free stars at redshifts as low as $z = 3$ (~ 2 Gyr after the Big Bang) is particularly important given observations of the Lynx arc – a star forming region at $z = 3.4$ with a Population III-consistent ionization source (Fosbury et al. 2003); and LLS1249 – a dense gas cloud at $z = 3.5$ with a Population III remnant metallicity (Crighton et al. 2016).

---

[2] Solar metallicity taken as $Z_\odot = 0.01$ to the nearest order of magnitude.

A renewed interest in direct detection of individual Population III stars has developed in anticipation of observations with the next generation of ground- and space-based facilities, in particular the recently launched James Webb Space Telescope (JWST). Using the Main Sequence properties of Population III stars from the evolutionary calculations in Schaerer (2002) and new metal-free model atmospheres calculated with the `TLUSTY` code (Hubeny & Lanz 1995), Rydberg et al. (2013) estimated the observable properties of isolated primordial stars at a range of redshifts and stellar masses. Without gravitational lensing, Population III stars appear far too faint to be detected even at the lowest redshift ($z = 2$) and in extremely long exposures (100 hr). Rydberg et al. (2013) also considered the case of a favorable lensed observation through the galaxy cluster MACS J0717.5+3745 – one of the largest gravitational lenses known (Zitrin et al. 2009). Even in the lensed case, a realistic detection was found to require either an extremely heavy Population III candidate ($\geq$ 300 $M_\odot$) or a primordial star formation rate, far in excess of theoretical expectation.

However, very high magnifications (μ) may be attained for brief periods of time in the event of gravitational lensing during a caustic transit. A caustic is the locus of points in the source plane where the determinant of the magnification matrix vanishes, i.e. where a true point source would experience infinite magnification (Narayan & Wallington 1992). A compact light source such as an individual star crossing a caustic may experience extreme magnification up to $\mu \sim 10^7$ from a lensing cluster with a continuous distribution of mass under most favorable conditions (Miralda-Escude 1991). In practice, microlenses within the galaxy cluster will distort the lens caustics, reducing the maximum magnification to $\mu \sim 10^4$ (Diego et al. 2018; Diego 2019).

Since larger magnifications require more favorable and increasingly less likely configurations, the true expected magnification in any given survey will strongly depend on the redshift of interest, the number of observable targets, and the scope of the survey itself. For example, Zackrisson et al. (2015) calculate $\mu \gtrsim 700$ as a realistic magnification estimate for detecting Population III stars in a 100 deg^2 ultra-deep survey. Extreme lensing events with $\mu \gg 10^3$ have allowed for recent discoveries of the most distant individual stars known at $z = 1.5$ ("*Icarus*", $\mu > 2000$, Kelly et al. 2018), $z = 2.7$ (currently unnamed, $\mu \gtrsim 10^4$, Chen et al. 2022) and $z = 6.2$ ("*Earendel*", $\mu > 4000$, Welch et al. 2022a,b). It has been suggested that the last source may in fact be a Population III star (Schauer et al. 2022).

Adopting more optimistic magnifications of $\mu \sim 10^4 - 10^5$, Windhorst et al. (2018) used new metal-free evolutionary tracks calculated with the `MESA` (`M`odules for `E`xperiments in `S`tellar `A`strophysics) code (Paxton et al. 2011, 2013, 2015, 2018, 2019) and assumed blackbody emergent spectra to characterize Population III stars in the context of future observations with JWST. The study estimated that a decade-long observational program monitoring up to 30 candidate lensing clusters will be required for a reliable detection.

In this study, we contribute to the ongoing effort of predicting future observations of Population III stars using stellar modelling. In particular, we focus on primordial stars with initial masses between 1 $M_\odot$ and $\sim 10^3$ $M_\odot$ on the Zero Age Main Sequence (ZAMS). ZAMS properties of Population III stars provide a lower bound on observability since later evolutionary stages are intrinsically more luminous and subjected to less interstellar absorption due to redder colors (Schaerer 2002; Windhorst et al. 2018). Additionally, the lower surface gravities of post-ZAMS stars may lead to super-Eddington luminosities in high-mass candidates, requiring detailed modelling of mechanical motion in the atmosphere that falls beyond the scope of this study (however, see Liu et al. 2021; Yoon et al. 2012).

We present theoretical color-magnitude diagrams of ZAMS Population III stars in JWST NIRCam filters for a broad range of redshifts based on new metal-free evolutionary models and model atmospheres. The observable properties of primordial stars are analyzed for their dependence on individual opacity sources and non-equilibrium distribution of the radiation field throughout the atmosphere. In particular, we demonstrate that even in the absence of non-grey opacity sources, Population III atmospheres cannot be approximated as blackbodies and always require detailed modelling. The calculated metal-free physical parameters on ZAMS are compared to their metal-poor counterparts and matched to simple, physically-motivated analytic relationships. The models are also evaluated in the context of the Eddington limit, that is of particular importance at high initial masses.

In this paper, Section 2 describes our modelling toolkit and presents the new atmosphere and evolutionary models calculated in this study. The key physical properties of Population III stars inferred from the models, such as the dependence of stellar evolution on the dominant energy production mechanism and the Eddington limit, are discussed in this section as well. Section 3 details our color-magnitude calculations at high redshift and presents the predicted color-magnitude and mass-magnitude relationships for Population III stars in the context of future JWST observations with gravitational lensing. The effect of cosmological parameters on our predictions is also estimated in Section 3. The key findings and important shortcomings of this investigation are summarized in Section 4. Population III model parameters are tabulated in Appendix A.

2. MODELING

2.1. *Overview of the methodology*

In this study, predictions of colors and magnitudes of Population III stars are drawn from synthetic photometry of metal-free stellar models at ZAMS. Each model is parameterized exclusively by the initial stellar mass and must account for all relevant physical processes governing the evolution of the star from its pre-Main Sequence (PMS) phase until steady-state hydrogen fusion. Synthetic photometry is obtained from the evolved emergent spectrum of the star, which is, in turn, calculated by solving the radiative transfer equation at every wavelength throughout the outer layers of the model comprising the stellar atmosphere.

Stellar atmospheres are particularly challenging to model due to the presence of neutral and partially ionized species, resulting in complex, wavelength-dependent opacity from significant non-grey contributions of bound-free and bound-bound sources. At high effective temperatures and extremely low metallicities considered in this work, the effect of non-grey atmospheric opacity on the structure of the stellar interior is expected to be insignificant, avoiding the need for detailed opacity calculations in the evolutionary models. However, the atmospheric opacity must be re-introduced into the model when calculating the final emergent spectrum of the star. We therefore calculate all models in multiple stages. First, evolutionary modelling was carried out from PMS to ZAMS with grey atmospheric opacity. The evolved stellar radii and luminosities were used to derive simple analytic relationships between stellar mass and the ZAMS surface parameters (effective temperature, T_{eff}, and surface gravity, $\log_{10}(g)$). Finally, the analytic relationships were evaluated at a broad range of stellar masses (from 1 $M_{\odot}$ to 1000 $M_{\odot}$) and the resulting surface parameters were used as inputs to dedicated model atmosphere calculations with the full opacity treatment and spectral synthesis.

2.2. *Evolutionary Modeling*

We calculated all evolutionary models with the `MESA` code (Paxton et al. 2011, 2013, 2015, 2018, 2019), version 15140. Evolutionary calculations in `MESA` are carried out in adaptive time steps until the chosen termination condition is met. By default, structure equations at each step are solved using the grey atmosphere optical depth-temperature relationship as the surface boundary condition. As demonstrated in our previous work (Gerasimov et al. 2022), this approximation is satisfactory at effective temperatures (T_{eff}) above 5000 K – a condition met by all models considered in this study.

In all evolutionary models, we chose to use $Y = 0.25$ as the approximation for the primordial helium mass fraction based on the Planck measurement in Planck Collaboration et al. (2020), taken to the nearest percent to match the default precision in `MESA`.

At initial masses below 90 $M_{\odot}$, models are initialized as PMS with a central temperature of 5×10^5 K (following Choi et al. 2016; Gerasimov et al. 2022), uniform chemical composition, and a density profile that satisfies the structure equations and results in the desired stellar mass. At significantly larger initial masses, a convergent PMS solution may not exist. Instead, the 90 $M_{\odot}$ PMS is used as the starting point and the mass is slowly increased to the required value using the mass relaxation routine provided by `MESA`. As an example, at the initial mass of 1000 $M_{\odot}$, the relaxation process lasts ≈ 1300 yr and results in an object with the central temperature of 72.7×10^6 K.

We extract the ZAMS luminosity and stellar radius from all evolutionary models once their nuclear power output begins to exceed 90% of the total luminosity. The sensitivity of the derived ZAMS parameters on the primordial helium mass fraction (Y) as well as the adopted PMS settings was estimated by computing multiple models at the representative initial masses of 10 $M_{\odot}$ and 1000 $M_{\odot}$ for a range of Y values from 0.24 to 0.26; a range of initial central temperatures from 3×10^5 K to 7×10^5 K; and a range of maximum (pre-relaxation) PMS masses from 50 $M_{\odot}$ to 100 $M_{\odot}$ (stored in the `max_mass_to_create` variable of the `build_pre_ms_model()` subroutine). We found the effect of PMS settings to not exceed 0.002 dex in both luminosity and radius at ZAMS. The effect of the chosen Y value was slightly larger, reaching 0.02 dex at lower masses. However, neither of the aforementioned uncertainties exceeds the average accuracy of the calculated analytic mass-radius and mass-luminosity relationships (to be introduced below) that were estimated as 0.02 dex and 0.03 dex respectively. Therefore, our results are insensitive to the input parameters within the aforementioned ranges.

We calculated 428 evolutionary models with initial stellar masses ranging from 1 $M_{\odot}$ to 1000 $M_{\odot}$ and used the ZAMS radii and luminosities to derive analytical mass-radius and mass-luminosity relationships for Population III stars. The input settings (inlist files) for all evolutionary models are available online[3]. Radii of main sequence stars are generally well-described by power law relations assuming that the dominant energy production and transport mechanisms do not vary significantly (Gimenez & Zamorano 1985; Lacy 1979; Demircan & Kahraman 1991). For stars with solar metallicity, the power law index changes noticeably around $\sim 1\ M_\odot$ due to the dissipation of the outer convective zone (Kippenhahn & Weigert 1994, Ch. 22.1) and the transition of the main hydrogen fusion mechanism from the proton-proton chain to the carbon-nitrogen-oxygen (CNO) cycle (Salaris & Cassisi 2005, Ch. 5.2). The latter effect is particularly important for zero-metallicity stars, as it is expected that enough carbon will be produced at sufficiently high masses to display a similar transition, thereby offsetting the power law break into the range of masses considered in this study. We therefore model the mass-radius relationship of ZAMS Population III stars as a broken power law with the break point mass ($M_{\rm bp}^{(R)}$) treated as a free parameter. The adopted relationship is

$$R \propto \begin{cases} M^{\alpha}, & \text{if } M \leq M_{\rm bp}^{(R)} \\ M^{\beta}, & \text{if } M > M_{\rm bp}^{(R)} \end{cases} \tag{1}$$

where M is the initial stellar mass, R is the corresponding stellar radius, and α and β are the proton-proton and CNO power indices respectively. The mass-luminosity (M–L) relationship is slightly more complicated due to the dependence on the dominant pressure support in the interior. High-mass ($M \gtrsim 10\ M_\odot$) stars behave approximately as Eddington standard models ($n = 3$ polytrope; Eddington 1918; Köhler et al. 2015) with the mass-luminosity power index gradually changing from ≥ 3 at $M \lesssim 100\ M_\odot$ to the asymptotic linear relationship ($L \propto M$) in the limit of $M \to \infty$. The transition occurs as the equation of state in the interior changes from the ideal gas law to radiation pressure dominance. To accommodate this additional complexity, we allow the index of the power law to change linearly with $\log_{10}(M)$ below some break point mass ($M_{\rm bp}^{(L)}$), which is treated as a free parameter, as before. The relationship is

$$L \propto \begin{cases} M^{\delta \log_{10}(M/M_\odot)+A}, & \text{if } M \leq M_{\rm bp}^{(L)} \\ M^{\gamma}, & \text{if } M > M_{\rm bp}^{(L)} \end{cases} \tag{2}$$

Here, L is the luminosity, γ is the high-mass power law index, δ is the rate of change of the index in the low-mass regime, and A is a constant, fixed by the requirement of the relationship to remain smooth around the break point,

$$A = \gamma - 2\delta \log_{10}\left(M_{\rm bp}^{(L)}/M_\odot\right) \tag{3}$$

The best-fit values of all six free parameters, as well as best-fit normalization factors, are given in Table 1. Note that the standard ZAMS mass-radius relationship for Population I (PI) stars has $\alpha_{\rm PI} \approx 0.8$ and $\beta_{\rm PI} \approx 0.57$ (Popper 1980, Kippenhahn & Weigert 1994, Ch. 22.1). While the high-mass index matches the Population III value in Table 1, the low-mass index is discrepant by a factor of ~ 4. This discrepancy arises because the energy production mechanism transition in Population I stars ($\approx 1.3\ M_\odot$; Salaris & Cassisi 2005, Ch. 5.2) very nearly coincides with the onset of convection in the envelope ($\sim 1\ M_\odot$), while Population III stars maintain radiative envelopes on either side of $M_{\rm bp}^{(R)}$. To compare Population III and Population I mass-luminosity relationships, we consider the average power law index in the $1 \leq M/M_\odot \leq 10$ and $1 \leq M/M_\odot \leq 40$ ranges. The standard values for Population I are 3.88 and 3.35 respectively (Popper 1980, Kippenhahn & Weigert 1994, Ch. 22.1), while the corresponding Population III values using Eq. 2 and Table 1 are 3.87 and 3.50, suggesting that the Population III relationship is nearly identical to its Population I counterpart at low masses and marginally steeper at higher masses.

The mass-radius relationship is plotted in Fig. 1 alongside the direct output from selected `MESA` models. For comparison, we also calculated multiple grids of `MESA` models at non-zero metallicities, whose mass-radius relationships are overplotted in the figure as well. The expected broken power law behavior is observed at all considered metallicities; however, the break point occurs at progressively decreasing stellar masses with increasing metallicity due to the larger initial carbon abundance. The point of equality in the energy production rates of the proton-proton chain and the CNO cycle is also indicated in the figure for every mass-radius relationship shown. Note that while the equality point is strongly correlated with the power law break point, the latter occurs at a lower stellar mass than the former as even a subdominant contribution from the CNO cycle is sufficient to influence the pressure structure within the star. In particular, we calculated the zero-metallicity equality point as $\approx 20.5\ M_\odot$ – over $4\ M_\odot$ higher than $M_{\rm bp}^{(R)}$.

The effective temperature ($T_{\rm eff}$) and surface gravity ($\log_{10}(g)$) are related to L, R and M according to Eqs. 4 (Stefan-Boltzmann law) and 5, where σ and G are the

---

[3] https://zenodo.org/record/7145568#.Yzzax33MLAU

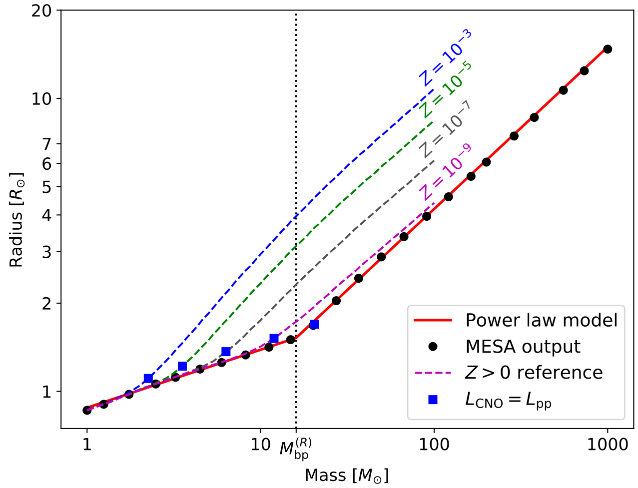

Figure 1. Mass-radius relationship from the metal-free evolutionary models calculated in this study alongside the best-fit power law approximation given in Eq. 1 and using the best-fit parameters in Table 1. Equivalent relationships for non-zero metallicities were calculated as well and are shown with dashed lines for comparison. Each dashed curve is parameterized by the total metal mass fraction, Z. The vertical line indicates the break in the best-fit power law relationship that originates from the onset of the CNO cycle in the core. The point where the energy production rates of the proton-proton chain ($L_{\rm pp}$) and the CNO cycle ($L_{\rm CNO}$) match is indicated with blue squares for every mass-radius relationship shown.

Table 1. Analytic fit parameters

Parameter	Value	Error	
α	0.1982	± 0.0019	
β	0.5527	± 0.0008	
$M_{\rm bp}^{(R)}$	16.03	± 0.11	$M_\odot$
R at 1 $M_\odot$	0.8792	± 0.0034	$R_\odot$
δ	-0.6893	± 0.0030	
γ	1.3137	± 0.0080	
$M_{\rm bp}^{(L)}$	153.0	± 2.8	$M_\odot$
L at 1 $M_\odot$	1.850	± 0.023	$L_\odot$

Stefan-Boltzmann and gravitational constants respectively.

$$T_{\rm eff} = \left(\frac{L}{4\pi\sigma R^2}\right)^{1/4} \tag{4}$$

$$\log_{10}(g) = \log_{10}\left(\frac{GM}{R^2\ [1\ {\rm cm\ s^{-2}}]}\right) \tag{5}$$

2.3. *Atmosphere Modeling*

Model atmospheres were calculated with version 9 of the `ATLAS` code (Kurucz 1970; Sbordone et al. 2004; Castelli 2005a; Kurucz 2014). The code attains high efficiency by sampling opacity from pre-tabulated opacity distribution functions (ODFs), described in Kurucz et al. (1974) and Carbon (1984). The `ATLAS` suite also contains the `DFSYNTHE` program (Castelli 2005b) that may be used to calculate ODFs for any given set of abundances, and the `SYNTHE` code (Kurucz & Avrett 1981) that computes the emergent spectrum from converged `ATLAS` models by sampling the opacity directly at the wavelengths of interest. All atmosphere models in this study were calculated at zero metallicity and with a more precise estimate of the primordial helium mass fraction, $Y = 0.2448$, adopted from Valerdi et al. (2021).

For this project, we developed a universal `Python` dispatcher that combines all three codes (originally written in `Fortran`) in a single user-friendly pipeline, complete with intermediate consistency checks and comprehensive documentation. Our dispatcher (Gerasimov & Larkin 2022) is available online[4].

`ATLAS` stratifies the atmosphere into 72 plane-parallel layers spanning the range of Rosseland mean optical depths (τ) from $\tau = 10^2$ at the bottom to $\tau = 10^{-7}$ at the top. For all models with stellar masses below 20 $M_\odot$, the ODFs were calculated following the "new" format (Castelli & Kurucz 2003) at 57 temperatures between $10^{3.3}$ K and $10^{5.3}$ K. At higher masses, the range fails to accommodate the deepest layers of the atmosphere that may exceed $10^{5.3}$ K in temperature. As such, a second set of ODFs was calculated with an extended upper temperature limit of $10^{5.85}$ K. For those calculations, the definition of the temperature grid stored in the variable `TABT` of the `LINOP()` subroutine in the `ATLAS` source code was modified according to the altered ODF format. Furthermore, the wavelength grid for opacity and radiation field sampling in `ATLAS`, that by default spans from ≈ 9 nm to 160 µm, had to be extended, first to 4 nm at stellar masses over 6 $M_\odot$, and then to 0.1 nm at stellar masses over 29 $M_\odot$. These extensions avoid errors in flux density and opacity integration due to significant contributions outside the default wavelength range. For each model, the adopted wavelength range was validated by ensuring that both the Planck function ($B_\nu(T)$) and its derivative (dB_ν/dT) drop below 0.1% of their maximum values at the wavelength range bounds in each layer of the atmosphere. The changes were applied to the `WBIG` variable in the `BLOCKR()` subroutine of `ATLAS`.

---

[4] https://github.com/Roman-UCSD/BasicATLAS

Atmosphere calculations in `ATLAS` are carried out through iterative improvements of an initial guess of the temperature profile throughout the atmosphere until a new profile is found that meets both the hydrostatic equilibrium condition for the prescribed surface gravity and the energy equilibrium condition for the prescribed effective temperature. On each iteration, the hydrostatic equilibrium condition is applied first to determine the pressure profile corresponding to the current temperature profile. Energy equilibrium is then evaluated throughout the atmosphere to determine corrections for the current temperature profile as well as the current percentage error in the flux and its derivative in each layer.

Since hydrostatic equilibrium is a hard requirement in `ATLAS`, no models can be calculated for stars above the Eddington limit – a critical luminosity (or, equivalently, critical effective temperature) above which the radiation pressure gradient begins to exceed gravitational attraction. To determine this limit, we considered the range of gravities between $\log_{10}(g) = 4.6$ and $\log_{10}(g) = 5.2$ and searched for the maximum effective temperature ($T_{\mathrm{eff}}^{\max}$) at which `ATLAS` is able to find a solution that is both in hydrostatic equilibrium and has flux and flux derivative errors below 1% over the course of 50 iterations using the grey temperature profile (Mihalas 1978, Ch. 3),

$$T(\tau) = T_{\mathrm{eff}} \left(\frac{3}{4}\tau + \frac{1}{2} \right)^{1/4} \tag{6}$$

as the initial guess, where $T(\tau)$ is the temperature at optical depth τ. The calculated values of $T_{\mathrm{eff}}^{\max}$ showed a nearly perfect exponential dependence on $\log_{10}(g)$ with deviations not exceeding 1% throughout the entire range of considered gravities. The functional form of the relationship is given by

$$\log_{10}(T_{\mathrm{eff}}^{\max}) = C_1 \log_{10}(g) + C_2 \tag{7}$$

where C_1 and C_2 are the best-fit parameters calculated as $C_1 = 0.2516 \pm 0.0013$ and $C_2 = 3.768 \pm 0.006$ for CGS units. Eq. 7 is directly comparable to the commonly adopted "classical" Eddington limit (Mihalas 1978, Ch. 7-2, Rybicki & Lightman 1986, Ch. 1, Beznogov et al. 2020) in CGS units, based on grey opacity dominated by Thomson scattering off electrons and local thermodynamic equilibrium (LTE):

$$\log_{10}(T_{\mathrm{eff}}^{\max}) = \frac{1}{4} \log_{10}(g) + \frac{1}{4} \log_{10} \left(\frac{c\rho}{\sigma n_e \sigma_T} \right) \tag{8}$$

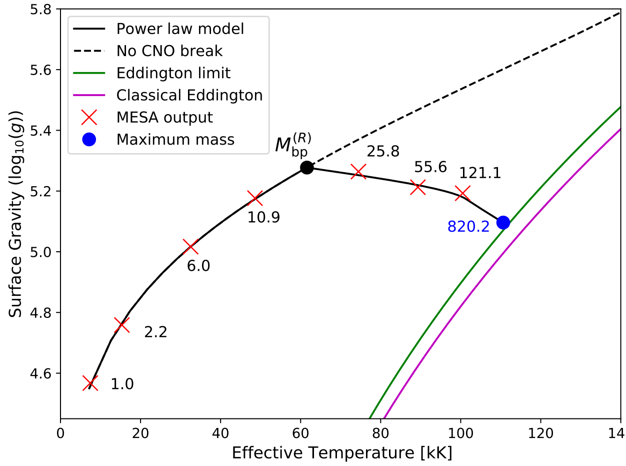

Figure 2. Surface parameters of ZAMS Population III stars compared to the exact calculation of the Eddington limit, including non-LTE effects and non-grey atmospheric opacity. The dashed curve traces out an alternative locus of surface parameters in the absence of the CNO break in the mass-radius relationship at $M_{\mathrm{bp}}^{(R)} \approx 16\ M_\odot$. Surface parameters extracted directly from selected `MESA` models are shown with red markers and labelled by the initial masses (in $M_\odot$). The maximum stellar mass with a convergent `ATLAS` atmosphere is shown with the blue circle at 820.2 $M_\odot$. The "classical" (grey atmosphere, LTE) Eddington limit from Eq. 8 is shown for reference. Note that the exact Eddington limit results in a lower maximum mass value.

Here, c is the speed of light, ρ is the mass density of the atmospheric layer, n_e is the corresponding electron number density, and σ_T is the Thomson scattering cross-section for an electron. When the layer is fully ionized, n_e/ρ only depends on the helium mass fraction:

$$\frac{n_e}{\rho} = 2\frac{Y}{m_{\mathrm{He}}} + \frac{1-Y}{m_{\mathrm{H}}} \tag{9}$$

where m_{He} and m_{H} are the helium and hydrogen atomic masses respectively. The "classical" equivalents of C_1 and C_2, denoted $C_1^{(T)}$ and $C_2^{(T)}$ respectively, can be evaluated numerically as $C_1^{(T)} = 0.25$ and $C_2^{(T)} = 3.795$. Since $C_1^{(T)} \approx C_1$ and $C_2^{(T)} > C_2$, the exact Eddington limit estimated with `ATLAS` is slightly lower than its "classical" counterpart at all considered surface gravities due to additional non-grey opacity sources and non-LTE effects in the atmosphere in the complete treatment.

Eq. 7 is plotted in Fig. 2 alongside the locus of surface parameters of ZAMS Population III stars derived from our analytic mass-radius and mass-luminosity relationships in Eqs. 1 and 2. The intersection between the two curves approximately represents the maximum mass of Population III stars with atmospheres in hydrostatic equilibrium, which also serves as the maximum initial stellar mass considered in this study. The maximum mass was calculated as 820.2 $M_\odot$ by gradually increasing the initial stellar mass of the model in increments of

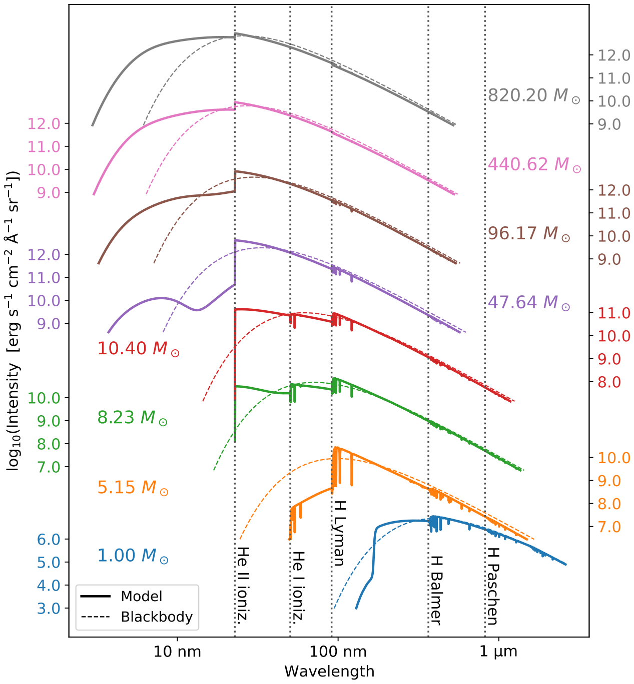

Figure 3. Synthetic spectra of ZAMS Population III stars for initial stellar masses between 1 $M_\odot$ and the Eddington limit (820.2 $M_\odot$). For clarity, each spectrum is shown on a separate color-coded vertical scale. The blackbody spectra at the corresponding effective temperatures are shown in dashes for reference. Important bound-free absorption breaks are highlighted with vertical lines and labelled.

0.1 $M_\odot$ until no convergent atmosphere solution could be found. Figure 2 emphasizes the importance of the CNO cycle in Population III stars, as the shape of the surface parameters locus is clearly dominated by the power law break in the derived mass-radius relationship at $M \approx 16\ M_\odot$.

Overall, we calculated 59 `ATLAS` atmospheres, logarithmically sampling the range of initial stellar masses between 1 $M_\odot$ and 820.2 $M_\odot$ and using the derived analytic relationships for surface parameters. For each model, the number of iterations was incremented in batches of 15 until the maximum flux error and the maximum flux derivative error dropped below the standard convergence requirements of 1% and 10% respectively (Sbordone & Bonifacio 2005; Mészáros et al. 2012; see Appendix A for details). Synthetic spectra for each model were then calculated with `SYNTHE` between 0.5 nm and 2.6 µm at the resolution of $\lambda/\delta\lambda = 6\times10^5$. The chosen wavelength range ensures that the flux density falls below 1% of its maximum value at the range bounds for all calculated model atmospheres. To account for the limited buffer size in `SYNTHE`, the spectral synthesis for all atmospheres was carried out in three batches: between 0.5 nm and 14 nm; between 14 nm and 400 nm; and between 400 nm and 2.6 µm. The calculations were run in parallel using the *Triton Shared Computing Cluster* (San Diego Supercomputer Center 2022). All calculated models are made public in our online repository[5]. The key properties of all models as well as their convergence parameters are tabulated in Appendix A.

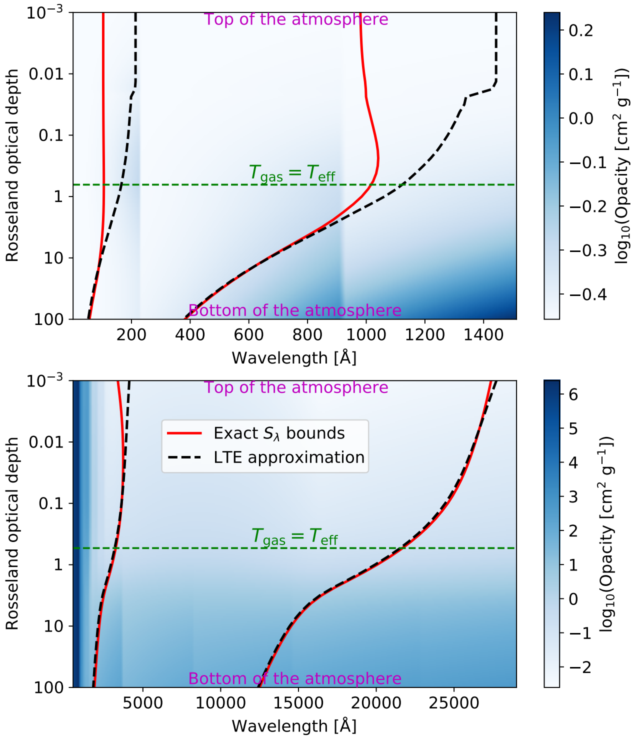

Figure 4. The 5th and the 95th percentiles of the wavelength distribution of the source function at a range of Rosseland mean optical depths for the solar atmosphere (*Bottom*) and a near-Eddington Population III atmosphere with $M = 820.2\ M_\odot$ (*Top*). The cases of the exact solution for the source function and the LTE approximation are shown in solid red and dashed black respectively. The optical depth where the gas temperature matches the effective temperature of the star is highlighted for reference. The background color scheme corresponds to the total atmospheric opacity as a function of both wavelength and Rosseland optical depth. The discontinuous changes in opacity are due to bound-free absorption breaks.

A few representative synthetic spectra are shown in Fig. 3. The spectra of stars with $M \gtrsim 50\ M_\odot$ display a considerable flux excess blueward of the He II ionization break (≈ 22.8 nm) compared to their corresponding blackbody profiles. Since ultraviolet emission is heavily attenuated by the interstellar medium in the early universe, this effect results in an overall reduction

---

[5] https://atmos.ucsd.edu/

of the observed brightness of Population III stars. The blue excess is primarily caused by non-LTE scattering of photons from deeper (and hotter) layers of the atmosphere. The departures from LTE in the radiation field are shown in Fig. 4 for the highest-mass Population III model considered in this study (820.2 $M_\odot$) as well as a solar atmosphere model ($T_{\rm eff} = 5770$ K, $\log_{10}(g) = 4.44$, abundances from Gerasimov et al. 2022). The figure shows the 5th and the 95th percentiles of the wavelength distribution of the source function (S_λ) for the case of LTE ($S_\lambda = B_\lambda$, no scattering) and the complete solution of the integral equation for S_λ (Mihalas 1978, Ch. 6-1). For the solar model, both cases are nearly indistinguishable in all but the outermost layers of the atmosphere that do not contribute to the emergent spectrum significantly. On the other hand, the departure from LTE is far more prominent in the Population III atmosphere, with a noticeable blue excess in the radiation field at Rosseland mean optical depths shallower than ~ 10.

The line features in Fig. 3 diminish at higher masses due to the reduced populations of neutral species in the atmosphere required for bound-bound absorption. Selected lines may appear stronger than shown here due to unaccounted higher-order NLTE effects (e.g. overpopulation of excited levels as described in Auer & Mihalas 1972), as captured in model sets with a more detailed treatment of NLTE line profiles (Bromm et al. 2001b; Rauch et al. 2018; Rydberg et al. 2013). However, the impact of narrow line features on broadband synthetic photometry is expected to be insignificant, especially in the JWST bands chosen in this study (see Section 3) that mostly occupy the comparatively line-free wavelength interval between the Lyman series of hydrogen and the Fowler series of ionized helium. To verify this claim, we recalculated our synthetic photometry (introduced in Section 3) with all line profiles artificially strengthened by the extreme factor of 10. We found that at stellar masses over 100 $M_\odot$, the predicted magnitudes do not deviate from their nominal values by more than 0.003 mag in the chosen JWST bands.

3. OBSERVABLE PARAMETERS

Color-magnitude diagrams (CMDs) in Fig. 5 and mass-magnitude relationships in Fig. 6 are provided for Population III stars in the most efficient JWST transmission bands. All synthetic photometry in this study was carried out in the `ABMAG` system (Oke & Gunn 1983) from the newly calculated synthetic spectra. For comparison, we also provide equivalent results for blackbody atmospheres at the corresponding effective temperatures.

3.1. *High-redshift synthetic photometry*

In `ABMAG`, the apparent magnitude, $m_{\rm AB}$, is calculated from the observed spectrum as:

$$m_{AB} = -2.5\log_{10}\left(\frac{\int(\nu)^{-1}f_\nu(\nu)e(\nu)d\nu}{\int 3631\ \mathrm{Jy}\ (\nu)^{-1}e(\nu)d\nu}\right) \tag{10}$$

Here, $f_\nu(\nu)$ is the apparent flux density per unit frequency, $e(\nu)$ is the efficiency of the instrument, and the integrals are evaluated over all frequencies (ν) in the frame of reference of the observer. The factor of $(\nu)^{-1}$ is included to adapt the relationship to a photon-counting instrument (Bohlin et al. 2014). Equivalently, Eq. 10 may be written in terms of the observed wavelength, λ, to match the output of `SYNTHE`:

$$m_{AB} = -2.5\log_{10}\left(\frac{\int \lambda f_\lambda(\lambda)e(\lambda)d\lambda}{\int 3631\ \mathrm{Jy}\ (\lambda)^{-1}e(\lambda)c d\lambda}\right) \tag{11}$$

At high redshift, the apparent flux density, f_λ, in Eq. 10 and Eq. 11 is derived from the modelled surface flux density, F_λ:

$$f_\lambda(\lambda) = F_\lambda(\lambda_{\rm e})T(\lambda, z)\frac{R^2}{(1+z)D_L^2} \tag{12}$$

(e.g. see Blanton & Roweis 2007), where $\lambda_{\rm e} = \lambda/(1+z)$ is the emitted wavelength at redshift z, R is the radius of the star and D_L is the luminosity distance to the star. In the equation, $T(\lambda, z)$ is the integrated transmissivity of the interstellar medium across the line of sight to the source. In the wavelength range of interest, the most significant contributions to interstellar attenuation are the bound-free and bound-bound absorption by ground state neutral hydrogen at $\lambda_{\rm e} \leq 1215.67$ Å – the Lyman α wavelength.

The photons absorbed by the interstellar medium will be re-emitted at longer wavelengths. Depending on the dynamical evolution of the medium under radiative feedback and the spatial density of Population III stars, this reprocessed radiation may contribute significantly to the observed spectrum of the star or have low impact on direct observations due to dilution over large surface areas (e.g. compare “type A” and “type C” environments in Zackrisson et al. 2011; also see Greif et al. 2009). In this study, we focus on the purely stellar spectra; however, see Rydberg et al. (2013); Sibony et al. (2022); Tumlinson et al. (2003); Kitayama et al. (2004) for various approaches to detailed feedback modelling.

At $z \leq 7$, we adopt $T(\lambda, z)$ from the numerical simulation in Meiksin (2006). At higher redshifts, the ab-

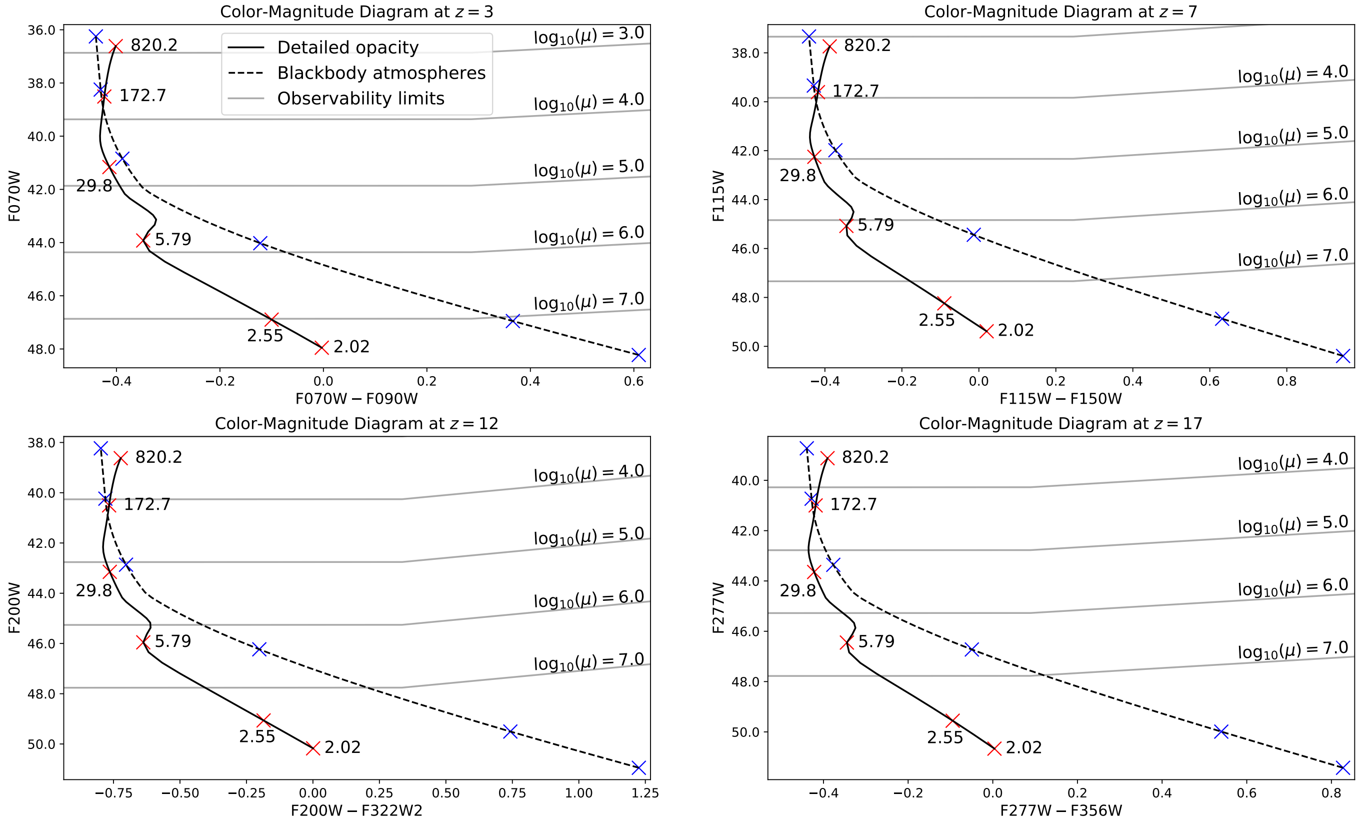

Figure 5. Color-magnitude diagrams of ZAMS Population III stars in the most optimal JWST bands listed in Table 2 at four different redshifts. Synthetic photometry is shown for both detailed opacity calculations based on model atmospheres and the corresponding blackbody profiles. Selected initial stellar masses are indicated in both cases with red and blue markers respectively. The red markers are labelled in solar masses. The blue markers correspond to the same masses as the red markers in the same order along the color-magnitude curve. Observability limits for JWST are shown in grey and labelled with the required gravitational lensing magnification, μ.

sorption by neutral hydrogen is sufficiently strong to be well-approximated by a hard cut-off:

$$T(\lambda, z; z > 7) \approx \begin{cases} 0, & \text{if } \lambda \leq (1+z)\ 1215.67\,\text{Å} \\ 1, & \text{otherwise} \end{cases} \tag{13}$$

As will be demonstrated, even at redshifts below $z = 7$ considered in this study, the most appropriate JWST bands for detecting Population III stars have blue cutoffs at $\lambda_e \gtrsim 1215.67$ Å, thereby ensuring that Eq. 13 remains a good approximation at all considered redshifts.

The luminosity distance, D_L, is calculated as a function of redshift as:

$$D_L = (1+z)c \int_0^z \frac{1}{H(z')} dz' \tag{14}$$

(Dodelson 2003, Ch. 2.2) where $H(z')$ is the Hubble parameter (Dodelson 2003, Ch. 2.4):

$$H^2(z) = H_0^2 \left(\Omega_r (1+z)^4 + \Omega_M (1+z)^3 + \Omega_\Lambda \right) \tag{15}$$

In Eq. 15, H_0 is the Hubble constant and Ω_r, Ω_M and Ω_Λ are the fractional present-day contributions of radiation (including relativistic matter), non-relativistic matter, and dark energy, respectively. We adopt the Hubble constant value of $H_0 = 67.4$ km s^{-1} Mpc^{-1} and $\Omega_M = 0.315$ in accordance with Planck Collaboration et al. (2020). The universe is assumed to be flat ($\Omega_\Lambda = 1 - \Omega_r - \Omega_M$) and Ω_r is calculated as (Dodelson 2003, Ch. 2.4.4):

$$\Omega_r = \left(1 + \frac{7}{8} \left(\frac{4}{11} \right)^{\frac{4}{3}} N_{\text{eff}} \right) \frac{4\sigma}{c^3} \frac{T_{\text{CMB}}^4}{\rho_{\text{crit}}} \tag{16}$$

We adopt $N_{\text{eff}} = 3.04$ (Mangano et al. 2002) as the effective number of neutrino flavors, $T_{\text{CMB}} = 2.725$ K (Fixsen 2009) as the present day temperature of the cosmic microwave background, and $\rho_{\text{crit}} = 3/(8\pi G) H_0^2$ as the critical density of the universe. The calculation implicitly assumes massless neutrinos. The accuracy of these cosmological assumptions is examined in Section 3.4.

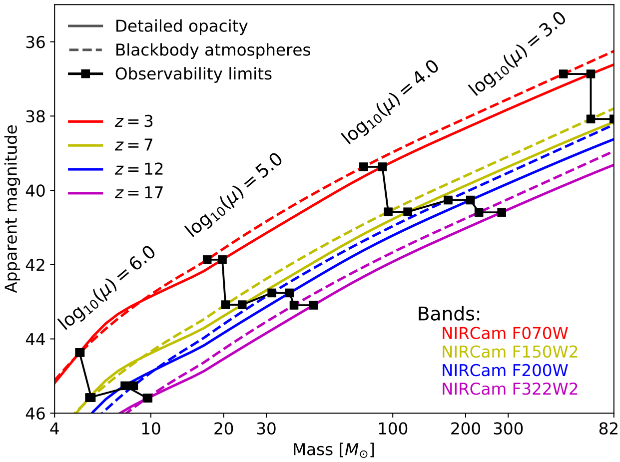

Figure 6. Mass-magnitude relationships for ZAMS Population III stars in the most optimal JWST bands listed in Table 2 at four different redshifts, color-coded. Note that a different band is used at each redshift. The equivalent relationships for the corresponding blackbody profiles are shown in dashed lines for comparison. The observability limits for JWST are indicated with black markers for each relationship shown. The displayed observability limits are grouped by the required gravitational lensing magnitification, μ.

3.2. *Choice of bands*

This study considers detecting Population III stars with JWST at $z \in (3, 7, 12, 17)$. The chosen range spans between the redshift of the predicted saturation of the Population III star formation rate in Xu et al. (2013) and the redshift of the candidate Population III ionization source in Fosbury et al. (2003). If the aim of the experiment is a simple detection of a Population III candidate in a single band, the optimal observation band for each stellar mass and redshift may be chosen by seeking the largest value of the predicted signal-to-noise ratio. At the lowest stellar masses, this condition will be met by a wide band, situated closest to the peak wavelength of the model spectrum. Due to extensive attenuation of flux by the interstellar medium at wavelengths shorter than the Lyman α, the optimal band at higher masses remains redward of the Lyman α in the observer's frame of reference instead of following the peak wavelength. The transition occurs around $\sim 10\ M_\odot$ for $z = 3$ and at $\lesssim 3\ M_\odot$ for $z \geq 7$. Since high-mass Population III stars are overwhelmingly more likely to be observable, the same high-mass optimal band may be safely employed for all Population III candidates at a given redshift.

We calculated the limiting magnitudes in all JWST Near Infrared Camera (NIRCam) and Mid-Infrared Instrument (MIRI) bands using the JWST Exposure Time Calculator (Pontoppidan et al. 2016) as the faintest magnitudes resulting in a signal-to-noise ratio of 3 in a $\sim$ 10 hr exposure (NIRCam: 20 groups, 9 integrations, `DEEP2` readout pattern; MIRI: 100 groups, 132 integrations, `FASTR1` readout pattern) for a flat frequency continuum. The best band for each redshift was chosen as the one corresponding to the smallest difference between the expected apparent magnitude of Population III stars in the high-mass regime and the limiting magnitude of the band. The chosen bands are listed in the "*Best single*" column of Table 2.

Table 2. Optimal bands for Population III detection

z	Best single	Best pair	
3	NIRCam `F070W`	NIRCam `F070W`	NIRCam `F090W`
7	NIRCam `F150W2`	NIRCam `F115W`	NIRCam `F150W`
12	NIRCam `F200W`	NIRCam `F200W`	NIRCam `F322W2`
17	NIRCam `F322W2`	NIRCam `F277W`	NIRCam `F356W`

Table 3. Limiting magnitudes

Band	Lim. mag	Band	Lim. mag
NIRCam `F070W`	29.3664	NIRCam `F090W`	29.6480
NIRCam `F150W2`	30.5796	NIRCam `F115W`	29.8404
NIRCam `F150W`	30.0816	NIRCam `F200W`	30.2616
NIRCam `F322W2`	30.5926	NIRCam `F277W`	30.2774
NIRCam `F356W`	30.3625		

Table 3. Calculated limiting magnitudes are listed for JWST bands in Table 2, assuming the detection signal-to-noise ratio of 3 in a $\sim$ 10 hr exposure (20 groups, 9 integrations, `DEEP2` readout pattern) of a flat frequency continuum.

A more detailed experiment may be designed with the aim of measuring the colors of Population III candidates in addition to simple detection, requiring a choice of two filters without significant overlap in their transmission profiles. We determine the optimal pairs of JWST filters for each redshift by considering all possible non-overlapping pairs of bands and choosing the one with the smallest *average* difference between the predicted magnitude of Population III candidates and the limiting magnitude of the band. As before, the choices are made in the high-mass regime. The resulting optimal pairs of filters are listed in the "*Best pair*" column of Table 2.

NIRCam bands were found to be most optimal for both simple detection and color measurements. The limiting magnitudes of all bands chosen in Table 2 are listed in Table 3.

3.3. *Results*

Predicted color-magnitude diagrams are presented in Fig. 5 for all four redshifts in the most optimal JWST band pairs listed in Table 2. Synthetic photometry for blackbody atmospheres at the same range of effective temperatures is shown in the figure as well for comparison. The overall trend of the color-magnitude relationship is nearly unchanged between redshifts, as the most efficient bands are placed in similar positions with respect to the redshifted energy density distribution predicted by the model atmospheres. At low masses ($M \lesssim 100\ M_\odot$), predicted colors shift blueward with increasing effective temperature, with the exception of a brief inversion of the trend around 6 $M_\odot$. We refer to this color-magnitude diagram feature as the "*helium loop*", as the inversion is caused by bound-free absorption of singly ionized helium in the second excited state ("Fowler break", $\lambda_\mathrm{e} = 205.1$ nm, Silberstein 1922). Once formed, the break disproportionately suppresses flux in the bluer band, resulting in the redder overall color.

In the high-mass regime ($M \gtrsim 100\ M_\odot$), the predicted color shifts redward with increasing temperature due to progressively decreasing contributions of free-free and bound-free opacities, both of which vary as λ^3 and, therefore, redistribute the flux towards shorter wavelengths. At high masses, Population III stars are predicted to be slightly fainter than blackbodies with identical effective temperatures due to the non-LTE distribution of the radiation field illustrated in Fig. 4.

Magnitude predictions for the most efficient single-band observations at each redshift are shown in Fig. 6 as functions of mass. Both Figs. 5 and 6 also contain the estimated JWST observability limits for different gravitational lensing magnifications, from $\mu = 10^3$ (approximate minimum required magnification for direct observations of Population III stars) to $\mu = 10^7$ (maximum theoretical magnification from Miralda-Escude 1991). The observability limits are based on the calculated limiting magnitudes in each band listed in Table 3.

3.4. *Cosmological parameters*

Predicted colors and magnitudes of Population III stars depend on the cosmological parameters adopted when calculating the luminosity distance, D_L (Eq. 14). Since D_L is independent of the physical properties of the star, the effect is identical for all initial masses. In this section, we estimate the magnitude of the effect for individual variations in the Hubble constant, H_0; the present-day matter contribution, Ω_M and the average neutrino mass, m_ν. The nominal value of each parameter adopted in this study, the considered range of variation, and the shift in the predicted magnitudes at the lower and upper bounds of the considered range are provided in Table 4. All tests are carried out at the largest considered redshift, $z = 17$, where the effect is expected to be most significant.

Table 4. Effect of cosmological parameters

	Adopted	Range		Effect [mag]	
	Value	Min	Max	Min	Max
H_0[a]	67.4	66.9	75.0	+0.02	−0.23
Ω_M	0.315	0.300	0.322	+0.04	−0.02
m_ν[b]	0.0	0.0	0.9	0.0	−0.15

[a] Hubble constant in km s^{-1} Mpc^{-1}

[b] Neutrino mass in eV c^{-2}, assumed identical for all neutrino species

For the Hubble constant, the adopted range spans from the lower error bound of the adopted nominal value (67.4 ± 0.5 km s^{-1} Mpc^{-1}, Planck Collaboration et al. 2020), based on Planck observations of the cosmic microwave background (CMB), to the upper error bound of the local Hubble constant estimate in Riess et al. (2016) (73.24 ± 1.74 km s^{-1} Mpc^{-1}), based on the updated distance calibration to type Ia supernovae.

The discrepancy between the CMB and local measurements of H_0, known as the *Hubble Tension*, depends on the adopted Ω_M prior. The two measurements have been shown to be consistent at 95% confidence for $\Omega_M \lesssim 0.3$ (Wei & Melia 2022). We therefore adopt $\Omega_M = 0.3$ as the lower bound on the variation range and take the error in the nominal value (0.315 ± 0.007, Planck Collaboration et al. 2020) as the upper bound.

To estimate the effect of massive neutrinos, we replace the relativistic neutrino density in Eq. 16 with the approximation for neutrinos with identical masses in Komatsu et al. (2011), implemented in `Astropy` (Astropy Collaboration et al. 2013, 2018). We adopted $m_\nu = 0.9$ eV c^{-2} as the maximum neutrino mass, measured in the Karlsruhe Tritium Neutrino (KATRIN) experiment (Katrin Collaboration et al. 2022).

As demonstrated in Table 4, H_0 and m_ν have the largest effect on the predicted photometry. Larger values for both parameters lead to shorter lookback times to a given redshift and, therefore, brighter apparent magnitudes of Population III stars. However, the gain in magnitude for both parameters was calculated to fall below 0.25 at the most extreme, which is expected to remain within the measurement uncertainty at the adopted limiting magnitude signal-to-noise ratio of 3.

4. CONCLUSION

In this study, we calculated new evolutionary models and model atmospheres for ZAMS Population III stars in hydrostatic equilibrium. The new models were used to investigate the physical properties of the first stars in the universe as well as to produce predictions of their colors and magnitudes as may be observed in the near future with JWST under strong gravitational lensing. The analysis was carried out at a broad range of plausible redshifts for Population III stars from $z = 3$ to $z = 17$. Our predictions of Population III color-magnitude diagrams and mass-magnitude relations are provided in Figs. 5 and 6 respectively. All predictions are given for the optimal JWST bands listed in Table 2. Our other findings are listed below:

- The mass-radius relationship of ZAMS Population III stars is well approximated by a broken power law, similar to their Population I counterparts. However, the break in the power law occurs at a much higher mass ($\approx 16\ M_\odot$ for Population III stars as opposed to $\approx 1\ M_\odot$ for Population I) due to the suppressed CNO cycle.

- Despite the initial absence of metals in Population III stars, the required amount of carbon to sustain the CNO cycle is produced at sufficiently high masses. The CNO cycle becomes the dominant energy production mechanism in Population III stars around $M \approx 20.5\ M_\odot$, in agreement with Yoon et al. (2012).

- The mass-luminosity relationship of ZAMS Population III stars may be approximated as a power law with a variable power index that decreases at higher masses. This behavior is observed in Population I stars as well and is approximately consistent with the Eddington standard model.

- The evolution of true metal-free stars is nearly indistinguishable from the evolution of extremely metal-poor stars with $Z \lesssim 10^{-9}$. This result is more conservative but consistent with the $Z = 10^{-8}$ limit derived in Windhorst et al. (2018). Furthermore, both values agree with the lower bound of the expected threshold of the Population III / Population II transition ($Z_{\text{cr}} \gtrsim 10^{-8}$; Omukai et al. 2005; Schneider et al. 2006; Clark et al. 2008).

- The maximum mass of ZAMS Population III stars, at which hydrostatic equilibrium is possible in the atmosphere (the Eddington limit) was calculated as $\approx 820\ M_\odot$. This value is well above the commonly considered range of initial masses for primordial stars, suggesting that hydrostatic equilibrium may be an adequate approximation in Population III models. The exact Eddington limit was found to be slightly lower than predicted by the classical formula (Eq. 8) due to non-grey opacity sources in the atmosphere as well as non-LTE effects. The influence of the CNO cycle on the internal structure of Population III stars was determined to be a key factor in setting the maximum mass.

- Atmospheres of high-mass Population III stars host strongly non-LTE radiation fields, resulting in significant excess in the UV flux compared to the corresponding blackbody profiles.

- The color-magnitude diagrams of Population III stars depend strongly on the non-grey opacity sources in the atmosphere with notable features including the "*helium loop*" at $M \sim 6\ M_\odot$ and the color-temperature inversion at $M \gtrsim 100\ M_\odot$. In general, ZAMS Population III stars are fainter than expected from blackbody profiles.

- At the lowest redshift ($z = 3$), the highest-mass Population III stars considered in this study ($M \gtrsim 700\ M_\odot$) are just observable with a gravitational lensing magnification of $\mu \sim 10^3$. A more plausible range of stellar masses ($M \gtrsim 100\ M_\odot$) would likely require $\mu \sim 10^4$. Such magnification is comparable to that inferred from previous detections of the most distant individual stars known (e.g. Welch et al. 2022a). At higher redshifts, the required magnification for an equivalent detection increases to $\mu \sim 10^5$.

- Our predictions of Population III observability do not depend significantly on the adopted cosmological parameters; however, the maximum calculated effect of ~ 0.25 mag is comparable to the adopted signal-to-noise ratio of JWST observations and may therefore be measurable under more generous gravitational lensing conditions than the minimum detection requirement considered in this study.

This study is limited to ZAMS Population III stars and may therefore be considered a lower limit on true JWST observability since later evolution stages are generally expected to be more luminous and less attenuated by the interstellar medium. The reduction in surface gravity during the post-main sequence evolution of Population III stars may drive the highest-mass stars considered in this study above the calculated Eddington limit, requiring a more detailed modelling approach allowing for mechanical motion in the atmosphere as well as mass loss.

In our predictions of the observational signatures of Population III stars, only radiation emitted directly from the stellar photospheres was considered. Realistic regions of Population III formation are likely to display significant flux contributions from the surrounding interstellar nebula. A follow-up study could deploy an analytic ionization model, as in Sibony et al. (2022), or a numerical simulation of radiative feedback, to derive the necessary corrections. In this context, the predictions drawn here may once again be interpreted as lower limits of the true observability of individual Population III sources.

While the detailed modelling of atmospheric opacity was shown to produce noticeably different results from the commonly adopted blackbody approximation (e.g. Windhorst et al. 2018; Fosbury et al. 2003), the quantitative difference in predictions of the two approaches will likely remain within the measurement uncertainty for Population III candidates at the observability threshold (e.g. at $z = 3$, the magnitude difference between the two approaches is ≈ 0.2 mag at the highest considered mass). However, the discrepancy may be detectable under marginally stronger gravitational lensing and should therefore be taken into account in more detailed observational studies of Population III stars.

Our overall result generally agrees with previous studies of Population III observability (e.g. Windhorst et al. 2018; Rydberg et al. 2013) that detection of the first stars in the universe may be possible with JWST under strong but realistic gravitational lensing, assuming sufficiently high stellar mass. Placing more specific constraints on the expected rate of detection remains challenging due to the highly debated initial mass function of Population III stars.

Finally, we note that Population III stars likely formed in clusters or galaxies rather than in isolation (e.g. Jaacks et al. 2019; Zackrisson et al. 2011; Johnson 2010; Johnson et al. 2009; DeSouza & Basu 2015; Visbal et al. 2017). The combined luminosity of such objects makes them more accessible targets, requiring less extreme gravitational lensing. However, modelling the spectral energy distributions of Population III clusters is further complicated by the dependency on the highly uncertain initial mass function and the concurrent formation of Population III and Population II stars (Xu et al. 2013; Wise et al. 2012b,a; Jaacks et al. 2019) at later epochs.

M. Larkin acknowledges funding support from the University of California at San Diego (UCSD) Department of Physical Sciences Summer Research Award and the UCSD Triton Research & Experiential Learning Scholars (TRELS) program. R. Gerasimov acknowledges funding support from HST Program GO-15096, provided by NASA through a grant from the Space Telescope Science Institute, which is operated by the Association of Universities for Research in Astronomy, Incorporated, under NASA contract NAS5-26555. This work was conducted at UCSD, which was built on the unceded territory of the Kumeyaay Nation. Today, the Kumeyaay people continue to maintain their political sovereignty and cultural traditions as vital members of the San Diego community. We acknowledge their tremendous contributions to our region and thank them for their stewardship.

Facilities: JWST (NIRCam, MIRI)

Software: `Astropy` (Astropy Collaboration et al. 2013, 2018), `Matplotlib` (Hunter 2007), `NumPy` (Harris et al. 2020), `SciPy` (Virtanen et al. 2020), `ATLAS` (Kurucz 1970; Sbordone et al. 2004; Castelli 2005a; Kurucz 2014), `DFSYNTHE` (Castelli 2005b), `SYNTHE` (Kurucz & Avrett 1981), `MESA` (Paxton et al. 2011, 2013, 2015, 2018, 2019)

APPENDIX

A. MODEL PARAMETERS

Table 5 lists the defining parameters and convergence criteria of all `ATLAS-9` model atmospheres calculated in this study. Initial masses are sampled logarithmically between 1 $M_\odot$ and the estimated Eddington limit (820 $M_\odot$). The corresponding stellar radii, luminosities, effective temperatures and surface gravities are calculated using Eqs. 1, 2, 4 and 5 as well as the best-fit parameters in Table 1. Only the effective temperature and surface gravity are used as inputs to model atmospheres. The final convergence is parameterized in terms of the maximum absolute flux error and the maximum absolute flux derivative error with respect to the depth-integrated mass density (see Kurucz 1970). Flux errors and flux derivative errors are used to calculate the temperature corrections between iterations using the Avrett & Krook (1963) scheme at large optical depths and the Λ-iteration scheme (Böhm-Vitense 1964, Mihalas 1978, Ch. 3-3) at shallow optical depths, respectively. All models calculated in this study meet the standard convergence target of flux error below 1% and flux derivative error below 10% (Sbordone & Bonifacio 2005; Mészáros et al. 2012).

Table 5. Parameters of Population III models calculated in this study

Initial Mass M [$M_\odot$]	Effective Temperature $T_{\rm eff}$ [K]	Surface gravity $\log_{10}(g)$	Radius R [$R_\odot$]	Luminosity $\log_{10}(L/L_\odot)$	Max Flux Error [%]	Max Flux Derivative Error [%]
1.000	7180	4.550	0.879	0.267	0.24	6.58
1.124	8047	4.581	0.900	0.485	0.62	1.54
1.264	9000	4.612	0.921	0.700	0.61	3.11
1.421	10045	4.642	0.942	0.911	0.71	7.49
1.597	11189	4.673	0.964	1.118	0.76	8.30
1.796	12437	4.704	0.987	1.322	0.78	7.88
2.019	13796	4.734	1.010	1.523	0.85	6.84
2.270	15273	4.765	1.034	1.719	0.79	5.00
2.551	16873	4.796	1.058	1.912	0.84	3.89
2.868	18602	4.827	1.083	2.102	0.74	4.94
3.225	20466	4.857	1.108	2.288	0.58	5.76
3.625	22472	4.888	1.134	2.471	0.53	5.73
4.075	24623	4.919	1.161	2.650	0.45	5.17
4.582	26924	4.949	1.188	2.825	0.35	4.50
5.151	29381	4.980	1.216	2.997	0.34	3.23
5.790	31996	5.011	1.245	3.165	0.31	1.63
6.510	34772	5.042	1.274	3.330	0.23	1.31
7.318	37712	5.072	1.304	3.491	0.24	0.93
8.227	40817	5.103	1.334	3.648	0.28	0.60
9.249	44087	5.134	1.365	3.802	0.31	0.65
10.398	47521	5.164	1.397	3.953	0.32	0.47
11.690	51118	5.195	1.430	4.100	0.32	0.36
13.141	54874	5.226	1.464	4.243	0.27	0.27
14.774	58785	5.256	1.498	4.383	0.24	0.23
16.609	62432	5.276	1.554	4.519	0.20	0.26

Table 5 *continued*

Table 5 *(continued)*

Initial Mass M [$M_\odot$]	Effective Temperature $T_{\rm eff}$ [K]	Surface gravity $\log_{10}(g)$	Radius R [$R_\odot$]	Luminosity $\log_{10}(L/L_\odot)$	Max Flux Error [%]	Max Flux Derivative Error [%]
18.672	65238	5.270	1.658	4.652	0.18	0.31
20.991	68031	5.265	1.769	4.781	0.17	0.46
23.598	70799	5.260	1.887	4.906	0.15	0.49
26.529	73528	5.254	2.013	5.028	0.12	0.56
29.825	76205	5.249	2.148	5.147	0.14	0.59
33.529	78819	5.243	2.291	5.261	0.15	0.70
37.694	81355	5.238	2.445	5.373	0.21	0.74
42.376	83800	5.233	2.608	5.480	0.26	0.75
47.639	86143	5.227	2.783	5.584	0.20	0.84
53.557	88369	5.222	2.969	5.685	0.22	1.09
60.209	90467	5.216	3.167	5.782	0.17	1.15
67.688	92425	5.211	3.379	5.875	0.21	1.08
76.095	94232	5.206	3.605	5.965	0.22	0.93
85.547	95878	5.200	3.846	6.052	0.23	0.69
96.172	97352	5.195	4.103	6.134	0.23	0.64
108.118	98647	5.189	4.378	6.214	0.23	0.65
121.547	99754	5.184	4.671	6.289	0.26	0.53
136.645	100666	5.179	4.983	6.361	0.31	0.45
153.617	101379	5.173	5.317	6.430	0.37	0.51
172.698	102000	5.168	5.672	6.497	0.44	0.59
194.149	102624	5.162	6.052	6.563	0.47	0.60
218.264	103253	5.157	6.456	6.630	0.40	0.49
245.375	103885	5.152	6.888	6.697	0.46	0.54
275.853	104521	5.146	7.349	6.764	0.32	0.38
310.117	105160	5.141	7.840	6.831	0.19	0.26
348.637	105804	5.136	8.365	6.898	0.13	0.26
391.941	106452	5.130	8.924	6.964	0.15	0.39
440.624	107103	5.125	9.521	7.031	0.18	0.43
495.354	107759	5.119	10.158	7.098	0.19	0.41
556.881	108419	5.114	10.838	7.165	0.22	0.44
626.052	109082	5.109	11.562	7.232	0.25	0.48
703.814	109750	5.103	12.336	7.299	0.30	6.53
791.234	110422	5.098	13.161	7.365	0.37	7.67
820.200	110629	5.096	13.425	7.386	0.60	4.59

REFERENCES

Abe, M., Yajima, H., Khochfar, S., Dalla Vecchia, C., & Omukai, K. 2021, MNRAS, 508, 3226, doi: 10.1093/mnras/stab2637

Abel, T., Bryan, G. L., & Norman, M. L. 2000, ApJ, 540, 39, doi: 10.1086/309295

Abohalima, A., & Frebel, A. 2018, ApJS, 238, 36, doi: 10.3847/1538-4365/aadfe9

Antonov, V. A., & Chernin, A. D. 1977, Astrofizika, 13, 271

Astropy Collaboration, Robitaille, T. P., Tollerud, E. J., et al. 2013, A&A, 558, A33, doi: 10.1051/0004-6361/201322068

Astropy Collaboration, Price-Whelan, A. M., Sipőcz, B. M., et al. 2018, AJ, 156, 123, doi: 10.3847/1538-3881/aabc4f

Auer, L. H., & Mihalas, D. 1972, ApJS, 24, 193, doi: 10.1086/190253

Avrett, E. H., & Krook, M. 1963, ApJ, 137, 874, doi: 10.1086/147564

Baade, W. 1944, ApJ, 100, 137, doi: 10.1086/144650

Bahcall, J. N., Flynn, C., Gould, A., & Kirhakos, S. 1994, ApJL, 435, L51, doi: 10.1086/187592

Bennett, C. L., Larson, D., Weiland, J. L., et al. 2013, ApJS, 208, 20, doi: 10.1088/0067-0049/208/2/20

Beznogov, M. V., Page, D., & Ramirez-Ruiz, E. 2020, ApJ, 888, 97, doi: 10.3847/1538-4357/ab5fd6

Blanton, M. R., & Roweis, S. 2007, AJ, 133, 734, doi: 10.1086/510127

Bohlin, R. C., Gordon, K. D., & Tremblay, P. E. 2014, PASP, 126, 711, doi: 10.1086/677655

Böhm-Vitense, E. 1964, SAO Special Report, 167, 99

Bond, H. E. 1980, in Bulletin of the American Astronomical Society, Vol. 12, 831

Bromm, V., Coppi, P. S., & Larson, R. B. 2002, ApJ, 564, 23, doi: 10.1086/323947

Bromm, V., Ferrara, A., Coppi, P. S., & Larson, R. B. 2001a, MNRAS, 328, 969, doi: 10.1046/j.1365-8711.2001.04915.x

Bromm, V., Kudritzki, R. P., & Loeb, A. 2001b, ApJ, 552, 464, doi: 10.1086/320549

Carbon, D. F. 1984, Line blanketing. (Cambridge University Press), 395–426

Castelli, F. 2005a, Memorie della Societa Astronomica Italiana Supplementi, 8, 25

—. 2005b, Memorie della Societa Astronomica Italiana Supplementi, 8, 34

Castelli, F., & Kurucz, R. L. 2003, in Modelling of Stellar Atmospheres, ed. N. Piskunov, W. W. Weiss, & D. F. Gray, Vol. 210, A20. https://arxiv.org/abs/astro-ph/0405087

Cen, R. 2003a, ApJ, 591, 12, doi: 10.1086/375217

—. 2003b, ApJL, 591, L5, doi: 10.1086/377068

Chen, W., Kelly, P. L., Treu, T., et al. 2022, arXiv e-prints, arXiv:2207.11658. https://arxiv.org/abs/2207.11658

Choi, J., Dotter, A., Conroy, C., et al. 2016, The Astrophysical Journal, 823, 102, doi: 10.3847/0004-637X/823/2/102

Clark, P. C., Glover, S. C. O., & Klessen, R. S. 2008, ApJ, 672, 757, doi: 10.1086/524187

Clark, P. C., Glover, S. C. O., Klessen, R. S., & Bromm, V. 2011, ApJ, 727, 110, doi: 10.1088/0004-637X/727/2/110

Cojazzi, P., Bressan, A., Lucchin, F., Pantano, O., & Chavez, M. 2000, MNRAS, 315, L51, doi: 10.1046/j.1365-8711.2000.03670.x

Crighton, N. H. M., O'Meara, J. M., & Murphy, M. T. 2016, MNRAS, 457, L44, doi: 10.1093/mnrasl/slv191

Demircan, O., & Kahraman, G. 1991, Ap&SS, 181, 313, doi: 10.1007/BF00639097

DeSouza, A. L., & Basu, S. 2015, MNRAS, 450, 295, doi: 10.1093/mnras/stv523

Diego, J. M. 2019, A&A, 625, A84, doi: 10.1051/0004-6361/201833670

Diego, J. M., Kaiser, N., Broadhurst, T., et al. 2018, ApJ, 857, 25, doi: 10.3847/1538-4357/aab617

Dodelson, S. 2003, Modern Cosmology (Academic Press)

Eddington, A. S. 1918, ApJ, 48, 205, doi: 10.1086/142427

Fixsen, D. J. 2009, ApJ, 707, 916, doi: 10.1088/0004-637X/707/2/916

Fosbury, R. A. E., Villar-Martín, M., Humphrey, A., et al. 2003, ApJ, 596, 797, doi: 10.1086/378228

Freese, K. 2017, International Journal of Modern Physics D, 26, 1730012, doi: 10.1142/S0218271817300129

Fuller, G. M., Woosley, S. E., & Weaver, T. A. 1986, ApJ, 307, 675, doi: 10.1086/164452

Gerasimov, R., Burgasser, A. J., Homeier, D., et al. 2022, ApJ, 930, 24, doi: 10.3847/1538-4357/ac61e5

Gerasimov, R., & Larkin, M. 2022, Roman-UCSD/BasicATLAS: v1.0.0, v1.0.0, Zenodo, doi: 10.5281/zenodo.7145514

Gimenez, A., & Zamorano, J. 1985, Ap&SS, 114, 259, doi: 10.1007/BF00653969

Graff, D. S., & Freese, K. 1996, ApJL, 467, L65, doi: 10.1086/310195

Greif, T. H., Glover, S. C. O., Bromm, V., & Klessen, R. S. 2010, ApJ, 716, 510, doi: 10.1088/0004-637X/716/1/510

Greif, T. H., Johnson, J. L., Klessen, R. S., & Bromm, V. 2009, MNRAS, 399, 639, doi: 10.1111/j.1365-2966.2009.15336.x

Greif, T. H., Springel, V., White, S. D. M., et al. 2011, ApJ, 737, 75, doi: 10.1088/0004-637X/737/2/75

Haiman, Z., & Loeb, A. 1997, ApJ, 483, 21, doi: 10.1086/304238

Harris, C. R., Millman, K. J., van der Walt, S. J., et al. 2020, Nature, 585, 357, doi: 10.1038/s41586-020-2649-2

Heger, A., & Woosley, S. E. 2002, ApJ, 567, 532, doi: 10.1086/338487

Herrington, N. P., Whalen, D. J., & Woods, T. E. 2022, arXiv e-prints, arXiv:2208.00008. https://arxiv.org/abs/2208.00008

Hirano, S., Hosokawa, T., Yoshida, N., Omukai, K., & Yorke, H. W. 2015, MNRAS, 448, 568, doi: 10.1093/mnras/stv044

Hirano, S., Hosokawa, T., Yoshida, N., et al. 2014, ApJ, 781, 60, doi: 10.1088/0004-637X/781/2/60

Hosokawa, T., Omukai, K., Yoshida, N., & Yorke, H. W. 2011, Science, 334, 1250, doi: 10.1126/science.1207433

Hubeny, I., & Lanz, T. 1995, ApJ, 439, 875, doi: 10.1086/175226

Hunter, J. D. 2007, Computing in Science and Engineering, 9, 90, doi: 10.1109/MCSE.2007.55

Jaacks, J., Finkelstein, S. L., & Bromm, V. 2019, MNRAS, 488, 2202, doi: 10.1093/mnras/stz1529

Johnson, J. L. 2010, MNRAS, 404, 1425, doi: 10.1111/j.1365-2966.2010.16351.x

—. 2015, MNRAS, 453, 2771, doi: 10.1093/mnras/stv1815

Johnson, J. L., Greif, T. H., Bromm, V., Klessen, R. S., & Ippolito, J. 2009, MNRAS, 399, 37, doi: 10.1111/j.1365-2966.2009.15158.x

Kashlinsky, A. 2005, ApJL, 633, L5, doi: 10.1086/498243

Kashlinsky, A., Arendt, R. G., Mather, J., & Moseley, S. H. 2005, in American Astronomical Society Meeting Abstracts, Vol. 207, American Astronomical Society Meeting Abstracts, 100.02

Katrin Collaboration, Aker, M., Beglarian, A., et al. 2022, Nature Physics, 18, 160, doi: 10.1038/s41567-021-01463-1

Keller, S. C., Bessell, M. S., Frebel, A., et al. 2014, Nature, 506, 463, doi: 10.1038/nature12990

Kelly, P. L., Diego, J. M., Rodney, S., et al. 2018, Nature Astronomy, 2, 334, doi: 10.1038/s41550-018-0430-3

Kinugawa, T., Inayoshi, K., Hotokezaka, K., Nakauchi, D., & Nakamura, T. 2014, MNRAS, 442, 2963, doi: 10.1093/mnras/stu1022

Kippenhahn, R., & Weigert, A. 1994, Stellar Structure and Evolution (Springer Berlin / Heidelberg)

Kitayama, T., Yoshida, N., Susa, H., & Umemura, M. 2004, ApJ, 613, 631, doi: 10.1086/423313

Kogut, A. 2003, NewAR, 47, 977, doi: 10.1016/j.newar.2003.09.029

Köhler, K., Langer, N., de Koter, A., et al. 2015, A&A, 573, A71, doi: 10.1051/0004-6361/201424356

Komatsu, E., Smith, K. M., Dunkley, J., et al. 2011, ApJS, 192, 18, doi: 10.1088/0067-0049/192/2/18

Kowalska, I., Bulik, T., & Belczynski, K. 2012, A&A, 541, A120, doi: 10.1051/0004-6361/201118604

Kurucz, R. L. 1970, SAO Special Report, 309

—. 2014, in Determination of Atmospheric Parameters of B-, A-, F- and G-Type Stars (Springer International Publishing), 39–51, doi: 10.1007/978-3-319-06956-2_4

Kurucz, R. L., & Avrett, E. H. 1981, SAO Special Report, 391

Kurucz, R. L., Peytremann, E., & Avrett, E. H. 1974, Blanketed model atmospheres for early-type stars (Smithsonian Astrophysical Observatory)

Lacy, C. H. 1979, ApJ, 228, 817, doi: 10.1086/156908

Larson, R. B. 1998, MNRAS, 301, 569, doi: 10.1046/j.1365-8711.1998.02045.x

Liu, B., & Bromm, V. 2020, MNRAS, 497, 2839, doi: 10.1093/mnras/staa2143

Liu, B., Sibony, Y., Meynet, G., & Bromm, V. 2021, MNRAS, 506, 5247, doi: 10.1093/mnras/stab2057

Madau, P., & Silk, J. 2005, MNRAS, 359, L37, doi: 10.1111/j.1745-3933.2005.00031.x

Maio, U., Ciardi, B., Dolag, K., Tornatore, L., & Khochfar, S. 2010, MNRAS, 407, 1003, doi: 10.1111/j.1365-2966.2010.17003.x

Maio, U., Petkova, M., De Lucia, G., & Borgani, S. 2016, MNRAS, 460, 3733, doi: 10.1093/mnras/stw1196

Mangano, G., Miele, G., Pastor, S., & Peloso, M. 2002, Physics Letters B, 534, 8, doi: 10.1016/S0370-2693(02)01622-2

Meiksin, A. 2006, MNRAS, 365, 807, doi: 10.1111/j.1365-2966.2005.09756.x

Mészáros, S., Allende Prieto, C., Edvardsson, B., et al. 2012, AJ, 144, 120, doi: 10.1088/0004-6256/144/4/120

Mihalas, D. 1978, Stellar atmospheres (W. H. Freeman)

Miralda-Escude, J. 1991, ApJ, 379, 94, doi: 10.1086/170486

Muñoz, V., Takhistov, V., Witte, S. J., & Fuller, G. M. 2021, JCAP, 2021, 020, doi: 10.1088/1475-7516/2021/11/020

Muratov, A. L., Gnedin, O. Y., Gnedin, N. Y., & Zemp, M. 2013, ApJ, 773, 19, doi: 10.1088/0004-637X/773/1/19

Narayan, R., & Wallington, S. 1992, in Gravitational Lenses, ed. R. Kayser, T. Schramm, & L. Nieser, Vol. 406 (Springer, Berlin, Heidelberg), 12, doi: 10.1007/3-540-55797-0_76

Nordlander, T., Bessell, M. S., Da Costa, G. S., et al. 2019, MNRAS, 488, L109, doi: 10.1093/mnrasl/slz109

Oke, J. B., & Gunn, J. E. 1983, ApJ, 266, 713, doi: 10.1086/160817

Omukai, K., Tsuribe, T., Schneider, R., & Ferrara, A. 2005, ApJ, 626, 627, doi: 10.1086/429955

Paxton, B., Bildsten, L., Dotter, A., et al. 2011, ApJS, 192, 3, doi: 10.1088/0067-0049/192/1/3

Paxton, B., Cantiello, M., Arras, P., et al. 2013, ApJS, 208, 4, doi: 10.1088/0067-0049/208/1/4

Paxton, B., Marchant, P., Schwab, J., et al. 2015, ApJS, 220, 15, doi: 10.1088/0067-0049/220/1/15

Paxton, B., Schwab, J., Bauer, E. B., et al. 2018, ApJS, 234, 34, doi: 10.3847/1538-4365/aaa5a8

Paxton, B., Smolec, R., Schwab, J., et al. 2019, ApJS, 243, 10, doi: 10.3847/1538-4365/ab2241

Planck Collaboration, Ade, P. A. R., Aghanim, N., et al. 2016, A&A, 594, A13, doi: 10.1051/0004-6361/201525830

Planck Collaboration, Aghanim, N., Akrami, Y., et al. 2020, A&A, 641, A6, doi: 10.1051/0004-6361/201833910

Pontoppidan, K. M., Pickering, T. E., Laidler, V. G., et al. 2016, in Society of Photo-Optical Instrumentation Engineers (SPIE) Conference Series, Vol. 9910, Observatory Operations: Strategies, Processes, and Systems VI, ed. A. B. Peck, R. L. Seaman, & C. R. Benn, 991016, doi: 10.1117/12.2231768

Popper, D. M. 1980, ARA&A, 18, 115, doi: 10.1146/annurev.aa.18.090180.000555

Rauch, T., Demleitner, M., Hoyer, D., & Werner, K. 2018, MNRAS, 475, 3896, doi: 10.1093/mnras/sty056

Riess, A. G., Macri, L. M., Hoffmann, S. L., et al. 2016, ApJ, 826, 56, doi: 10.3847/0004-637X/826/1/56

Rowan-Robinson, M. 1983, in Early Evolution of the Universe and its Present Structure, ed. G. O. Abell & G. Chincarini, Vol. 104, 109–112

Rybicki, G. B., & Lightman, A. P. 1986, Radiative Processes in Astrophysics (Wiley-VCH)

Rydberg, C.-E., Zackrisson, E., Lundqvist, P., & Scott, P. 2013, MNRAS, 429, 3658, doi: 10.1093/mnras/sts653

Salaris, M., & Cassisi, S. 2005, Evolution of Stars and Stellar Populations (John Wiley and Sons)

San Diego Supercomputer Center. 2022, doi: 10.57873/T34W2R

Santos, M. R., Bromm, V., & Kamionkowski, M. 2002, MNRAS, 336, 1082, doi: 10.1046/j.1365-8711.2002.05895.x

Sbordone, L., & Bonifacio, P. 2005, Atlas Cookbook. http://atmos.obspm.fr/index.php/documentation/7

Sbordone, L., Bonifacio, P., Castelli, F., & Kurucz, R. L. 2004, Memorie della Societa Astronomica Italiana Supplementi, 5, 93. https://arxiv.org/abs/astro-ph/0406268

Schaerer, D. 2002, A&A, 382, 28, doi: 10.1051/0004-6361:20011619

Schauer, A. T. P., Bromm, V., Drory, N., & Boylan-Kolchin, M. 2022, arXiv e-prints, arXiv:2207.02863. https://arxiv.org/abs/2207.02863

Schneider, R., Ferrara, A., Natarajan, P., & Omukai, K. 2002, ApJ, 571, 30, doi: 10.1086/339917

Schneider, R., Omukai, K., Inoue, A. K., & Ferrara, A. 2006, MNRAS, 369, 1437, doi: 10.1111/j.1365-2966.2006.10391.x

Schwarzschild, M., & Spitzer, L. 1953, The Observatory, 73, 77

Sharda, P., & Krumholz, M. R. 2022, MNRAS, 509, 1959, doi: 10.1093/mnras/stab2921

Sibony, Y., Liu, B., Simmonds, C., Meynet, G., & Bromm, V. 2022, arXiv e-prints, arXiv:2205.15125. https://arxiv.org/abs/2205.15125

Silberstein, L. 1922, Nature, 110, 247, doi: 10.1038/110247b0

Sokasian, A., Yoshida, N., Abel, T., Hernquist, L., & Springel, V. 2004, MNRAS, 350, 47, doi: 10.1111/j.1365-2966.2004.07636.x

Spergel, D. N., Verde, L., Peiris, H. V., et al. 2003, ApJS, 148, 175, doi: 10.1086/377226

Stacy, A., & Bromm, V. 2014, ApJ, 785, 73, doi: 10.1088/0004-637X/785/1/73

Stacy, A., Bromm, V., & Lee, A. T. 2016, MNRAS, 462, 1307, doi: 10.1093/mnras/stw1728

Stacy, A., Greif, T. H., & Bromm, V. 2012, MNRAS, 422, 290, doi: 10.1111/j.1365-2966.2012.20605.x

Susa, H., Hasegawa, K., & Tominaga, N. 2014, ApJ, 792, 32, doi: 10.1088/0004-637X/792/1/32

Suwa, Y., Takiwaki, T., Kotake, K., & Sato, K. 2007, ApJL, 665, L43, doi: 10.1086/521078

Trenti, M., Stiavelli, M., & Shull, J. M. 2009, ApJ, 700, 1672, doi: 10.1088/0004-637X/700/2/1672

Tumlinson, J., Shull, J. M., & Venkatesan, A. 2003, ApJ, 584, 608, doi: 10.1086/345737

Umeda, H., & Nomoto, K. 2002, ApJ, 565, 385, doi: 10.1086/323946

Valerdi, M., Peimbert, A., & Peimbert, M. 2021, MNRAS, 505, 3624, doi: 10.1093/mnras/stab1543

Virtanen, P., Gommers, R., Oliphant, T. E., et al. 2020, Nature Methods, 17, 261, doi: 10.1038/s41592-019-0686-2

Visbal, E., Bryan, G. L., & Haiman, Z. 2017, MNRAS, 469, 1456, doi: 10.1093/mnras/stx909

Wagner, R. L. 1978, A&A, 62, 9

Wei, J.-J., & Melia, F. 2022, ApJ, 928, 165, doi: 10.3847/1538-4357/ac562c

Welch, B., Coe, D., Diego, J. M., et al. 2022a, Nature, 603, 815, doi: 10.1038/s41586-022-04449-y

Welch, B., Coe, D., Zackrisson, E., et al. 2022b, arXiv e-prints, arXiv:2208.09007. https://arxiv.org/abs/2208.09007

Windhorst, R. A., Timmes, F. X., Wyithe, J. S. B., et al. 2018, ApJS, 234, 41, doi: 10.3847/1538-4365/aaa760

Wise, J. H., Abel, T., Turk, M. J., Norman, M. L., & Smith, B. D. 2012a, MNRAS, 427, 311, doi: 10.1111/j.1365-2966.2012.21809.x

Wise, J. H., Turk, M. J., Norman, M. L., & Abel, T. 2012b, ApJ, 745, 50, doi: 10.1088/0004-637X/745/1/50

Woods, T. E., Patrick, S., Elford, J. S., Whalen, D. J., & Heger, A. 2021, ApJ, 915, 110, doi: 10.3847/1538-4357/abfaf9

Wyithe, J. S. B., & Loeb, A. 2003, ApJ, 586, 693, doi: 10.1086/367721

Xu, H., Wise, J. H., & Norman, M. L. 2013, ApJ, 773, 83, doi: 10.1088/0004-637X/773/2/83

Yoon, S. C., Dierks, A., & Langer, N. 2012, A&A, 542, A113, doi: 10.1051/0004-6361/201117769

Yoshida, N., Omukai, K., Hernquist, L., & Abel, T. 2006, ApJ, 652, 6, doi: 10.1086/507978

Yung, L. Y. A., Somerville, R. S., Finkelstein, S. L., et al. 2020, MNRAS, 496, 4574, doi: 10.1093/mnras/staa1800

Zackrisson, E., González, J., Eriksson, S., et al. 2015, MNRAS, 449, 3057, doi: 10.1093/mnras/stv492

Zackrisson, E., Rydberg, C.-E., Schaerer, D., Östlin, G., & Tuli, M. 2011, ApJ, 740, 13, doi: 10.1088/0004-637X/740/1/13

Zitrin, A., Broadhurst, T., Rephaeli, Y., & Sadeh, S. 2009, ApJL, 707, L102, doi: 10.1088/0004-637X/707/1/L102